NIH Public Access
Author Manuscript
Med Eng Phys. Author manuscript; available in PMC 2013 January 01.

Published in final edited form as:
Med Eng Phys. 2012 January ; 34(1): 64–77. doi:10.1016/j.medengphy.2011.06.019.

Automatic segmentation of radiographic fiducial and seeds from X-ray images in prostate brachytherapy

Nathanael Kuo[a], **Anton Deguet**[b], **Danny Y. Song**[c], **Everette C. Burdette**[d], **Jerry L. Prince**[e], and **Junghoon Lee**[e]

[a]Department of Biomedical Engineering, Johns Hopkins University, Baltimore, MD, USA

[b]Department of Computer Science, Johns Hopkins University, Baltimore, MD, USA

[c]Department of Radiation Oncology, Johns Hopkins University, Baltimore, MD, USA

[d]Acoustic MedSystems Inc., Champaign, IL, USA

[e]Department of Electrical and Computer Engineering, Johns Hopkins University, Baltimore, MD, USA

Abstract

Prostate brachytherapy guided by transrectal ultrasound is a common treatment option for early stage prostate cancer. Prostate cancer accounts for 28% of cancer cases and 11% of cancer deaths in men with 217,730 estimated new cases and 32,050 estimated deaths in 2010 in the United States alone. The major current limitation is the inability to reliably localize implanted radiation seeds spatially in relation to the prostate. Multimodality approaches that incorporate X-ray for seed localization have been proposed, but they require both accurate tracking of the imaging device and segmentation of the seeds. Some use image-based radiographic fiducials to track the X-ray device, but manual intervention is needed to select proper regions of interest for segmenting both the tracking fiducial and the seeds, to evaluate the segmentation results, and to correct the segmentations in the case of segmentation failure, thus requiring a significant amount of extra time in the operating room. In this paper, we present an automatic segmentation algorithm that simultaneously segments the tracking fiducial and brachytherapy seeds, thereby minimizing the need for manual intervention. In addition, through the innovative use of image processing techniques such as mathematical morphology, Hough transforms, and RANSAC, our method can detect and separate overlapping seeds that are common in brachytherapy implant images. Our algorithm was validated on 55 phantom and 206 patient images, successfully segmenting both the fiducial and seeds with a mean seed segmentation rate of 96% and sub-millimeter accuracy.

Keywords

prostate brachytherapy; seed localization; X-ray; non-isocentric C-arm; fiducial; segmentation; overlapping seeds

© 2011 Institute of Physics and Engineering in Medicine. All rights reserved.

Corresponding Author: Junghoon Lee, Ph.D., Department of Electrical and Computer Engineering, Johns Hopkins University, 201A Clark Hall, 3400 North Charles Street, Baltimore, MD 21218, Phone: (410) 516-6820, Fax: (410) 516-5566, junghoon@jhu.edu.

Publisher's Disclaimer: This is a PDF file of an unedited manuscript that has been accepted for publication. As a service to our customers we are providing this early version of the manuscript. The manuscript will undergo copyediting, typesetting, and review of the resulting proof before it is published in its final citable form. Please note that during the production process errors may be discovered which could affect the content, and all legal disclaimers that apply to the journal pertain.

Conflict of Interest Statement
None.

NIH-PA Author Manuscript
NIH-PA Author Manuscript
NIH-PA Author Manuscript

NIH-PA Author Manuscript

NIH-PA Author Manuscript

NIH-PA Author Manuscript

1. Introduction

Prostate cancer is a serious health concern in North America, accounting for 28% of all newly diagnosed cancers among men in the United States while remaining among the most fatal of cancers [1]. Efforts are continually made to diagnose prostate cancer at its early stage and treat it effectively. One of the several treatment options available today is low dose rate (LDR) brachytherapy, a procedure involving the permanent implantation of numerous (~100) small radioactive sources known as seeds into the prostate. LDR brachytherapy is a very effective means to treating prostate cancer, and has in fact become a common choice because of its excellent long-term treatment outcomes of maximizing cancer control while minimizing morbidity [2].

LDR brachytherapy is used to treat about 55,000 patients annually in the U.S. Although generally popular among patients, the American Brachytherapy Society suggests there is potential to improve prostate brachytherapy, particularly in performing intraoperative treatment planning (ITP) and delivery [3]. Traditionally, a transrectal ultrasound (TRUS) prostate volume study is performed a few weeks before the brachytherapy surgery to determine an individual treatment plan for the patient. However, many alterations occur between the planning study and the implantation procedure, including changes in prostate shape, patient positioning, and overall setup. Brachytherapy has therefore been moving towards ITP—i.e., a process of creating and/or updating the treatment plan inside the operating room (OR) in order to eliminate the disadvantages of the preplanning method. A major current limitation of ITP, however, is the difficulty in correctly, rapidly, and automatically localizing currently implanted seeds in relation to the prostate. This prevents the computation of current dose distribution based on existing seed positions, thereby preventing quantitatively informed dynamic revision of the treatment plan during surgery. If fast and accurate dose computation based on intraoperative images were available, a truly optimized brachytherapy procedure would be possible, thereby further maximizing cancer control and minimizing morbidity. Unlike HDR (high dose rate) brachytherapy, LDR does not provide an opportunity for temporal modulation of the dose distribution and is totally dependent upon accuracy of seed placement in the prostate. The localization of brachytherapy seeds therefore plays a critical role in improving treatment for prostate cancer patients.

Seed localization is a challenging task. While the seed positions can be estimated by the treatment plan or by localizing the needle tips visualized in the TRUS images when implanting the seeds into the prostate, such estimates are inaccurate for various reasons. First, the seeds can naturally migrate in the soft tissue of the prostate. Secondly, the prostate itself can deform due to patient movement, needle insertion, or edema caused by the procedure. Finally, the surgeon can place seeds imprecisely during implantation. Direct image-based seed localization is also difficult since TRUS is limited in its ability to visualize the seeds due to noise and multipath scattering caused by the numerous seeds. In order to overcome these obstacles, various researchers have proposed multi-modality approaches that include X-rays to localize the seeds in relation to the prostate. However, most of these approaches require very expensive X-ray imaging systems such as radiation therapy simulators [4, 5] or CT scanners [6, 7] for accurate seed reconstruction, thus requiring dedicated suites or specific setups that are not typically used for this procedure and are prohibitive in cost. In addition, the position of the patient is very different inside the imaging gantry compared to the position during the implant procedure, thus making the registration between the X-ray and TRUS volumes challenging. On the other hand, Jain et al. [8] have proposed an alternative system that uses the ubiquitous non-isocentric mobile C-arm to complement TRUS. In their system, TRUS is used to image the prostate while 3 to 4

NIH-PA Author Manuscript

NIH-PA Author Manuscript

NIH-PA Author Manuscript

C-arm X-ray shots are taken at arbitrary poses to image the seeds, all while the patient is still positioned on the surgical table with his legs in a high lithotomy position. The three-dimensional (3-D) seed locations are reconstructed from these two-dimensional (2-D) X-ray images, which are subsequently registered to the TRUS prostate volume, making dynamic dose calculation possible. In order to achieve accurate tracking of the C-arm and registration with the TRUS frame, they mount a radiographic tracking fiducial called FTRAC [9] (see Fig. 1) to the needle-guiding template in a mechanically calibrated position, thereby providing a transformation between X-ray and TRUS.

The system proposed by Jain et al. [8] is very attractive as a practical solution for dynamic dose calculation, since it is cost-effective and can be easily adopted by minimally altering the contemporary TRUS-guided brachytherapy procedure. However, significant improvements can be made in the workflow of their system, especially in regards to segmentation. A key element to the described approach by Jain et al. is the fluoroscope tracking fiducial (FTRAC), a compact image-based tracking fiducial composed of radio-opaque beads (BBs), lines and ellipses (see Fig. 2). The FTRAC is designed to solve two important issues for localizing seeds: 1) the estimation of the C-arm pose for seed reconstruction and 2) registration to the prostate volume computed from TRUS images. However, while most other portions of the system are fully automatic, current segmentation algorithms of the FTRAC [10] and the seeds [11] require operator intervention, bringing the entire pipeline to a halt. The reason for this is that both the FTRAC and the seeds are located in the same X-ray field of view, and current algorithms require the operator to outline a region of interest (ROI) each for the FTRAC and for the seeds so that these features can be processed separately. Even with properly selected ROIs, such algorithms often need further intervention because of automatic segmentation failure, in which case the operator has to manually correct or entirely resegment the features. There are several alternative seed segmentation algorithms available [12, 13], but none would eliminate the need of user intervention since they also require the selection of an ROI in this framework. Overall, these drawbacks inhibit the workflow of ITP, which is problematic in the OR where time is of critical importance.

In this paper, we propose an ROI-free segmentation of both the radiographic tracking fiducial and the seeds. The purpose of this work is two-fold: 1) to accomplish fully automatic pipelining from image acquisition to seed reconstruction by removing the requirement of selecting ROIs, and 2) to minimize manual intervention caused from automatic segmentation failures. Although we focus on the segmentation of the FTRAC in this paper, our methods can be easily applied to various radiographic tracking fiducials that use points, lines, or conics [14, 15].

2. Methods

Our proposed algorithm (see Fig. 3) takes as input a single X-ray grayscale image and outputs the equations of the lines, the 2-D image coordinates of the points, and the equations of the conics (note that the FTRAC has 3 parallel lines, 9 BBs, and 2 ellipses) as well as the 2-D image coordinates of the brachytherapy seeds. In cases when there are overlapping seeds in a projection view, the algorithm automatically classifies them as overlapping and outputs separated image coordinates. If desired, the resulting segmentation can be overlaid on the input image for visualization (see Fig. 4). There are several assumptions made regarding the X-ray image, all of which are practical in the clinical setting: 1) the X-ray image has been corrected for geometric image distortion caused by the X-ray image intensifier, 2) the FTRAC and seeds are fully visible within the X-ray field of view (FOV), 3) the FTRAC appears to the right of the seeds without overlapping them, 4) the FTRAC is oriented upright, and 5) the TRUS probe is retracted and therefore not located in the FOV.

NIH-PA Author Manuscript

NIH-PA Author Manuscript

NIH-PA Author Manuscript

Our algorithm was tested on Palladium-103 seeds which tend to appear small and oval in X-ray.

2.1. Morphological image processing

As mathematical morphology [16] has proven fast and effective for segmenting various features such as points and edges, we first review morphological operations that are frequently applied to both binary and grayscale images in our segmentation process. The following four translation invariant morphological operations are especially important, forming a basis for other morphological operations. In these definitions, f is the input image and B is the structuring element.

$$\text{Erosion:}\quad \psi_\varepsilon(f)(x,y)=\min_{\xi,\eta}[f(x+\xi,y+\eta)-B(\xi,\eta)] \quad (1)$$

$$\text{Dilation:}\quad \psi_\delta(f)(x,y)=\max_{\xi,\eta}[f(x-\xi,y-\eta)+B(\xi,\eta)] \quad (2)$$

$$\text{Opening:}\quad \psi_\delta(\psi_\varepsilon(f))(x,y) \quad (3)$$

$$\text{Closing:}\quad \psi_\varepsilon(\psi_\delta(f))(x,y) \quad (4)$$

Erosion and dilation can be described as nonlinear shape filters that replace a pixel with the minimum and maximum, respectively, of its neighborhood as indicated by a shaped structuring element. Opening and closing are standard combinations of erosion and dilation that are often used for filtering by shape.

There are also more advanced morphological operations used in our algorithm:

$$\text{Conditional dilation:}\quad \delta_B^k(f^m|f)=\delta_B^1\delta_B^1\ldots\delta_B^1(f^m|f)\,k \text{ times, where } \delta_B^1(f^m|f)=\min[\psi_\delta(f^m),f] \quad (5)$$

$$\text{Reconstruction:}\quad r_B(f^m|f)=\max_{k>1}[\delta_B^k(f^m|f)] \quad (6)$$

$$\text{Top-hat:}\quad f-\psi_\delta(\psi_\varepsilon(f)) \quad (7)$$

$$\text{Top-hat by reconstruction:}\quad f-r_B(\psi_\delta(\psi_\varepsilon(f))|f). \quad (8)$$

Conditional dilation is a stepwise region growing process, using repeated incremental dilations to grow the marker image f^m into the mask image f (note that every pixel in f^m must have a value less than or equal to that in f). It also provides a convenient means to describe morphological reconstruction, which is the end result of continuous conditional dilations. Top-hat is an operation involving the subtraction of an image by its opening, and is used to enhance contrast in an image. It can also be used along with reconstruction, hence top-hat by reconstruction, to provide more specific contrast depending on the structuring element. Fig. 5 shows an example illustrating conditional dilation and reconstruction. Note that a reconstructed image by definition is equivalent to an image after numerous conditional dilations. However, the outputted reconstructed image is not necessarily equivalent to the inputted mask image. This is related to the nature of the min function in conditional dilation. In areas where the mask image f is less than the dilation $\psi\delta(f^m)$, the mask image is chosen and thus reproduced; in other areas, the dilation is chosen rather than the mask and thus

NIH-PA Author Manuscript

NIH-PA Author Manuscript

NIH-PA Author Manuscript

appears differently from the mask. Fig. 6 shows an example of top-hat and top-hat by reconstruction. Note that these two operations often produce very different results.

The choice of structuring element (i.e., its size and shape) in these morphological operations depends on the object at hand. Since object size can vary depending on resolution and scale, the size of the structuring element must also adjust accordingly. However, once resolution and scale are fixed, the size of the structuring element may likewise remain fixed. Since object shape is not dependent on resolution or scale, the shape of the structuring element may remain constant regardless of these factors.

2.2. FTRAC Lines and BBs

The FTRAC has a fixed structure that can be exploited; in particular, the 9 FTRAC BBs are positioned by design coincidently on top of the 3 parallel FTRAC lines. This becomes the basis for our approach of segmenting the lines and BBs simultaneously.

The first objective is to obtain a clean binary image of the FTRAC BBs. To do so, we perform a top-hat by reconstruction operation using a disk-shaped structuring element on the complemented X-ray image and then binarize the image using Otsu's threshold [17] (see Fig. 7a). The connected components [18] in the resulting binary image are then analyzed by properties such as area (i.e. the number of pixels in a connected region), eccentricity, solidity, and location to filter out objects that are not BBs (such as the implanted brachytherapy seeds). The 9 FTRAC BBs are distinguished from the majority of seeds and other remaining structures in the image due to their larger size, rounder shape, and location to the right side of the image. The result is a binary image containing the FTRAC BBs and very few if any remaining false detections (see Fig. 7b).

Next, the FTRAC BBs are differentiated from false detections by the fact that they lie on lines that are oriented roughly in the vertical direction. To do this, the Hough transform [19] is applied to create a list of lines that pass through the pixels of the detected regions, sorted by their line strength. The FTRAC lines are always among the strongest lines output by the Hough transform since the BBs are large in size and since there are few false detections. The FTRAC lines are further distinguished because they comprise three lines that are parallel, roughly vertical, and are on the right side of the image (see Fig. 7c). Since the Hough transform parameter space is fairly coarse (to reduce computation time), the three line positions are further refined. In particular, the three lines are fit using least squares to line edges produced from a thresholded top-hat operator using a vertical structuring element applied to the complemented source image (see Fig. 7d). This process yields three precise equations for the three FTRAC lines appearing in the source image.

Given the FTRAC lines, false BB detections are removed by applying morphological reconstruction to the binary image (see Fig. 7b) using the intersections with the detected FTRAC lines as the marker image. The centroids of the resulting connected components give the estimated positions of the 9 FTRAC BBs.

2.3. FTRAC Ellipses

Segmentation of the FTRAC ellipses is much easier given knowledge of the positions of the FTRAC lines and BBs for two reasons: 1) a rough estimate of the regions of the FTRAC ellipses can be gained from the FTRAC lines and BBs, and 2) the FTRAC ellipse edges can be distinguished from the FTRAC line edges. Still, determining the equations of the FTRAC ellipses is still a challenging task as ellipse detection in itself is still an ongoing research field.

NIH-PA Author Manuscript

NIH-PA Author Manuscript

NIH-PA Author Manuscript

Our first objective in ellipse detection is to obtain a binary image containing the ellipse edges. Naïve application of the Canny edge detector [20] yields double edges rather than a desired single edge since the ellipse boundaries are spike edges rather than step edges. Instead, we apply Otsu's threshold to the result of a top-hat operation using a square structuring element on the complemented input image (see Fig. 8a). Further image processing follows, including 1) removing the edge pixels within a small range of the middle FTRAC line since it passes through the center of the two ellipses and thus interferes with ellipse detection, 2) filtering by area and shape using an opening with a square structuring element to remove spurious non-ellipse edges, and 3) thinning the edges of the binary image, which reduces complexity of ellipse detection by refining edges to have the width of a single pixel (see Fig. 8b). These operations and their corresponding parameters are applied uniformly to all images.

At this stage, we have a binary image containing thinned FTRAC ellipse edges as well as a few remaining false edges. From here, we estimate an approximate region for each of the two FTRAC ellipses so an ellipse detection algorithm can subsequently determine the equations of the two ellipses separately. To do so, we exploit the now known positions of the FTRAC BBs to define an outer boundary around the ellipses. A dividing line between the two ellipse regions is then found by a two step process: first, by randomly positioning lines parallel and in between the now known outermost FTRAC lines to search for lines with four intersections, presumably two intersections per ellipse; and second, by finding the average point between the two innermost intersections out of the four total intersections. Such an average point then defines a horizontal line to separate the two ellipse regions.

Just as with lines, there exists a Hough transform for detecting ellipses. However, the generalized Hough transform is impractical for this application since it requires a large amount of memory. As an alternative, we used an ellipse detection algorithm based on random sample consensus (RANSAC) [21], which is a technique to fit instances of a model (in our case, ellipses) to data even in the presence of numerous outliers. The RANSAC framework requires code for a model fitting method and an error distance measurement, both of which already exist in the case of ellipses. We therefore implemented our RANSAC-based ellipse detection algorithm with the aid of pre-existing code, including the numerically stable ellipse fitting algorithm developed by Halir and Flusser [22] and the point-to-ellipse distance calculation described by Xie and Ohya [23]. Using edge pixels selected within each of the previously estimated FTRAC ellipse regions, our ellipse detection algorithm then determines the equations of the two FTRAC ellipses.

2.4. Seeds

Segmentation of the FTRAC projection elements simplifies seed segmentation because the seeds can be distinguished from potentially similar appearing features of the FTRAC, such as the BBs. However, seed segmentation at this point is not trivial because: 1) other objects in the entire field of view can appear as seeds, and 2) seeds can overlap one another in the image making it difficult to identify their locations.

To segment the seeds we first obtain a binary image of the seeds by thresholding the top-hat by reconstruction of the complemented image using a disk-shaped structuring element (see Fig. 9a). We chose a disk-shaped structuring element over a rectangular-shaped one since seeds can appear in any orientation. After removing the FTRAC region using a bounding quadrilateral determined by the FTRAC BBs and lines, we are left with a binary image of the seeds and some spurious seed-like artifacts (see Fig. 9b). To remove these false positives, we take advantage of the fact that seeds are typically positioned close to one another. Therefore objects that are greater than an empirically determined threshold distance from the densest seed region are assumed to be false positives and removed from the binary

NIH-PA Author Manuscript

NIH-PA Author Manuscript

NIH-PA Author Manuscript

image. Such spurious detections are rare (and we do not see such an artifact in Fig. 9b) because the densest objects in the image are usually associated with either the seeds or the FTRAC BBs; but occasionally the urethral catheter used during surgery bends in such a way as to produce an artifact (see Fig. 13b), and this step is typically effective in removing it.

At this point we have a binary image comprising only seeds, but some of these seeds are overlapping. We identify overlapping seeds based on the following physical principle. Assume a single seed with uniform attenuation coefficient μ is placed in a radio-transparent medium. According to Beer's Law,

$$I(x,y)=I_0 e^{-\mu\int dz}$$

where $I(x, y)$ is the image intensity at position (x, y), I_0 is the original X-ray intensity, and z is orthogonal to the image plane along the line of projection. We can rearrange this equation to obtain:

$$-\ln\frac{I(x,y)}{I_0}=\mu\int dz$$

$$\iint -\ln\frac{I(x,y)}{I_0}dxdy=\mu\iiint dxdydz=\mu V$$

Here, V is the volume of a single seed and is clearly constant irrespective of the projection direction. Moreover, if there are n seeds in the projection, then the total volume is nV, and the resulting value to the double integral is $n\mu V$. Therefore the calculation of $\iint -\ln\frac{I(x,y)}{I_0}dxdy$ over each connected seed region of the image can serve as a metric for identify overlapping seeds, with the resulting value being constant for a single seed, double the constant for two overlapping seeds, triple for three seeds, and so forth.

There are several issues to consider when implementing this principle. First, seeds are not actually placed in a radio-transparent medium as described above since the patient anatomy surrounding the seeds has some degree of radio-opaqueness. Moreover, we generally do not know the value of the source intensity I_0. Nonetheless, the complemented top-hat by reconstruction that was previously calculated can effectively solve these two issues and represent $\frac{I(x,y)}{I_0}$ in this strategy. This is made possible since top-hat by reconstruction not only enhances contrast but removes nearly all background effects in the process. As a result, this emulates a normalized projection of seeds through a radio-transparent medium, evaluating to 1 at positions $(x, y)$where there is no seed and a value between 0 and 1 where there is a seed (see Fig. 9c). Another issue to consider is that the image is digital, so rather than calculate a double integral, we calculate a double summation. Finally, we also do not know the actual value of μV. However, this value can be estimated by taking the median value of this metric among all the connected regions, since in general the vast majority of regions are single seeds. Therefore, all seeds visible from regions with a metric value greater than a defined threshold are considered overlapped seeds, and these indications are included as an output of the algorithm.

The final step is to determine the positions of the individual seeds identified above to be in overlapping regions. We use the facts that palladium seeds in X-ray are small and appear Gaussian shaped in intensity (see Figs. 9d and 9e), and that the k-means [24] clustering algorithm works particularly well with Gaussian distributed data. Briefly, the k-means algorithm takes an array of data values (which might be vectors) as input and, given a user-

NIH-PA Author Manuscript

NIH-PA Author Manuscript

NIH-PA Author Manuscript

specified number of clusters, outputs the cluster means and the cluster classification for each data point. In our case, each pixel of a particular overlapping region is set up as a data point multiple times according to the intensity of that pixel. For example, if pixel (50,100) has intensity value of 128 in 256-grayscale, there would be 128 instances of the data point (50,100) in the input to k-means. The previously described metric also provides a good estimate for the number of seeds n found in an overlapping region and is therefore used as the number of clusters input to the k-means algorithm. The cluster means determined by k-means are the estimated positions of seeds found in overlapping regions. The positions of the remaining seeds found in non-overlapping regions are calculated by each region's centroid (see Fig. 9f).

Figs. 10–13 demonstrate a second example of the steps in our algorithm, this time for a clinical case that is also presented in our results.

3. Results

The algorithm was tested on 55 phantom and 206 clinical images. X-ray images were taken using an OEC 9600 (phantom images) and an OEC 9800 (clinical images) using an analog NTSC video output with an image size of 720×480 pixels and a pixel resolution of 0.44 mm × 0.44 mm. Although it is possible to use digital DICOM images, they are not universally supported in all C-arms and generally cannot be retrieved quickly in the OR.

The outputs of the algorithm were compared to manually corrected automatic segmentations of the FTRAC and the seeds. The manually corrected segmentation of the FTRAC was first computed using an automatic algorithm requiring an ROI [10]. Manual corrections followed, with the BBs segmented by choosing the nearest darkest points to the user's selected points, the lines by performing least squares fitting of the 5 points per line that the user selects, and the ellipses by least squares fitting of the 7 points per ellipse that the user selects. As with the FTRAC, the manually corrected segmentation of the seeds was first computed by an automatic algorithm requiring an ROI [11], and then followed by any manual corrections. All manual segmentations were done by a well trained operator who had hundreds of cases of experience segmenting the FTRAC and seeds. In the most difficult cases where it is unclear whether a seed is overlapped, multiple poses were examined to verify the correct manual segmentation. Automatic segmentations of both the FTRAC and the seeds in the proposed algorithm required 5 seconds per image on average when running on a PC with a 2.33 GHz Intel Core 2 Duo processor.

Differences between manually corrected and automatic segmentations of the FTRAC are included in Tables 1–4 and were calculated as follows. Let the subscripts m and a represent the manually corrected and automatic segmentations, respectively. BB segmentation differences are calculated using the Euclidean distance between the two BB coordinates, (x_m, y_m) and (x_a, y_a). For line segmentation differences, let ρ and θ represent the parameters for the equation of a line, such that

$$x \cos \theta + y \sin \theta = \rho.$$

The difference in perpendicular distance to origin is $|\rho_m - \rho_a|$ and the difference in angle is $|\theta_m - \theta_a|$. For ellipse segmentation differences, let h, k, a, b, θ be the parameters for the equation of an ellipse, such that

$$\frac{((x \cos \theta + y \sin \theta) - h)^2}{a^2} + \frac{((-x \sin \theta + y \cos \theta) - k)^2}{b^2} = 1.$$

NIH-PA Author Manuscript

NIH-PA Author Manuscript

NIH-PA Author Manuscript

The difference in center position is calculated as $\sqrt{(h_m - h_a)^2+(k_m - k_a)^2}$, the difference in major axis is $|a_m - a_a|$, the difference in minor axis is $|b_m - b_a|$, and the difference in orientation is $|\theta_m - \theta_a|$. Finally, for pose estimation differences, pose is calculated from the FTRAC segmentations using the pose recovery mathematics provided by Jain et al. [9] and is given in the homogeneous form

$$\begin{bmatrix} r_{11} & r_{12} & r_{13} & t_x \\ r_{21} & r_{22} & r_{23} & t_y \\ r_{31} & r_{32} & r_{33} & t_z \\ 0 & 0 & 0 & 1 \end{bmatrix},$$

where r_{ij} represents entries in the rotation matrix R, and t_i represents entries in the translation vector T. Difference in rotation angle is thus computed as $\cos^{-1}(\text{trace}(R_a R_m^{-1})/2)$, and translation difference is computed as $|t_m - t_a|$ for each of the three axes.

3.1. Phantom Experiments

A phantom was created with gelatin and implanted with 5 different seed configurations comprising 20, 40, 60, 80, 100, and 120 seeds, respectively. A total of 55 images (10 images for 20 seeds and 9 images for the other cases) were taken at various C-arm poses as would be done in a clinical setting (see Fig. 4).

For FTRAC segmentation, our algorithm was able to segment 53 of the 55 distortion corrected phantom images successfully, resulting in a 96.4% success rate. We define successful segmentation here as having less than 2 degrees difference in rotation angle compared to manually corrected segmentation, using pose as the standard since it is a simple unifying metric for all the feature segmentations of the FTRAC. Moreover, current reconstruction algorithms can handle pose errors of less than 2 degrees with greater than 97.5% success rate [25]. Segmentation failure can therefore result either by failing to produce segmentation outputs for all features, or by inaccurately segmenting features so large differences in rotation angle occur. A sample result is shown in Fig. 4, and differences in the successful automatic FTRAC segmentations of the phantom images and their manually corrected counterparts are shown in Tables 1–4.

For seed segmentation, our algorithm detected 3485 seeds while there were 3629 seeds. 3479 detected seeds from our algorithm matched to the manually corrected seeds, resulting in a 95.9% seed detection rate and a 0.2% false positive rate. More specific results are recorded in Table 5.

3.2. Clinical Study

A total of 206 patient images were collected from 7 patients under the Institutional Review Board's approved protocols at the Johns Hopkins Hospital. For all patients, Palladium-103 seeds (Theragenics®, GA, United States) were implanted. The X-ray images were taken at various C-arm poses, and the number of implanted seeds varied from 22 to 84 seeds (see Fig. 10).

44 of the 206 clinical images were not properly taken with the complete FTRAC in the field of view, therefore failing to satisfy one of the assumptions of our algorithm. Of the remaining 162 images, 143 FTRAC segmentations were successful resulting in an 88.3% success rate. A sample result is shown in Fig. 10, and quantitative differences between successful automatic and manually corrected segmentations are also shown in Tables 1–4 within the row or column labeled "Clinical".

NIH-PA Author Manuscript

NIH-PA Author Manuscript

NIH-PA Author Manuscript

For seed segmentation, 13 among the 143 images with successful FTRAC segmentations were improperly taken with the TRUS probe in the field of view, being useful for FTRAC segmentation development but inappropriate for seed segmentation evaluation. Consequently, in the remaining 130 images, our algorithm detected 7118 seeds while there were 7014 seeds. 6936 detected seeds in our algorithm matched to the manually corrected segmented seeds, resulting in a 98.9% seed detection rate but a 2.6% false positive rate. More specific results are also recorded in Table 5.

4. Discussion and Conclusion

We have developed an algorithm to simultaneously segment the FTRAC and the seeds while effectively identifying and separating overlapped seeds. The end result is a pipelined seed reconstruction system for prostate brachytherapy and minimized manual intervention caused by segmentation failures.

With the addition of this algorithm, processing begins immediately after image acquisition, so the steps of distortion correction, FTRAC segmentation, seed segmentation, and pose estimation are automatically pipelined. Once three images are acquired, seed reconstruction (using a technique described elsewhere [25]) completes the pipeline so that dose distribution calculations can be obtained. All computations are easily completed within the tens of seconds it takes for the technician to rotate the C-arm to the proper pose for acquiring the next X-ray image.

Although the algorithm fulfills its purpose, there are a few items that require caution. First, this algorithm uses the FTRAC fiducial, which is sensitive to segmentation differences along the depth (z) direction (see Table 4) and is not yet commonly used in brachytherapy procedures. However, since most fiducials are likewise composed of lines, BBs, and/or ellipses, there is high confidence that the fiducial segmentation techniques used in this algorithm can be generalized to other fiducials. Secondly, our algorithm was only tested for implants of Palladium-103 seeds, not for implants of Iodine-125 seeds that are also commonly used in many clinics. Since iodine seeds appear larger and more rectangular than palladium seeds under X-ray, it is unknown whether our algorithm will show similar segmentation performance on iodine seeds. However, it is important to note that the theory for segmenting palladium seeds and iodine seeds is similar, and the general steps of morphological processing, calculating the double summation, and applying k-means would likely be applicable to iodine seeds also. Finally, while this algorithm is able to resolve most overlapping seeds in projection images, it is unable to completely identify every seed in the image, especially in cases where one seed completely hides another. However, there are many existing matching-based [25, 26] and tomosynthesis-based [5, 27] reconstruction algorithms that can handle this “hidden seed” problem as well as the potential issue of reconstructing images with differing number of detected seeds.

A few algorithms have already been proposed for seed segmentation. Tubic et al. [12] have proposed a seed segmentation algorithm similarly based on morphological processing while also resolving overlapped seeds. However, there are several key differences between our work and theirs, including the choice in automatic threshold selection, overlapped seed analysis, and approach for resolving overlapped seeds. While we apply Otsu’s threshold, a double summation metric, and k-means, Tubic et al. uses the bidimensional entropy method, analysis by connected region properties, and simulated annealing. Our work has a higher seed detection rate than their algorithm, boasting higher than a 96% detection rate compared to their 92% detection rate. Su et al. [13] have also proposed a seed segmentation algorithm. In their work, they have resolved overlapped seeds through a simulation study using Gaussian classifiers and geometric analysis of clusters. Although they have done extensive

NIH-PA Author Manuscript

NIH-PA Author Manuscript

NIH-PA Author Manuscript

work on simulation and phantom studies, they have not presented any clinical results. Moreover, they present segmentation and cluster analysis time of 1 minute per projection.

While our algorithm is not perfect, it certainly improves the current workflow. At their worst, previous algorithms would require the operator to travel back and forth from C-arm to console, impeding with the multiple responsibilities of operating the C-arm, specifying ROIs, inspecting the results, and manually correcting segmentations, which can take as much as several additional minutes in the OR. Even at their best, they would still require the operator to divert attention away from orienting the C-arm and towards managing ROIs on the computer. On the other hand, at its best, our algorithm would allow the operator to focus almost exclusively on the C-arm, only requiring him to take a glance from his position at the C-arm to verify the results, and being limited only by his speed in C-arm operation. Even at its worst, the operator always has the option to take another X-ray image at a slightly adjusted C-arm position to allow the pipeline another chance to run successfully, or he can manually correct segmentation errors as would be needed in the case of failure regardless of segmentation algorithm.

We have presented our work for simultaneously segmenting the FTRAC and brachytherapy seeds. Through innovative use of image processing techniques, our method is able to give satisfactory results for both FTRAC and seed segmentation. Moreover, image acquisition and preprocessing based on X-ray is pipelined without need for manual intervention, saving crucial time in the OR and improving dynamic dosimetry system performance.

Acknowledgments

This work was supported by grants DoD W81XWH-05-1-0407, NIH/NCI 2R44CA099374, and NIH/NCI 1R01CA151395.

References

1. Jemal A, Siegel R, Xu J, Ward E. Cancer statistics, 2010. CA: A Cancer Journal for Clinicians. 2010:60. (published online: Jul. 7, 2010, doi: 10.3322/caac.20073).
2. Koukourakis G, Kelekis N, Armonis V, Kouloulias V. Brachytherapy for prostate cancer: a systematic review. Advances in Urology. 2009
3. Nag S, Ciezki JP, Cormack R, Doggett S, DeWyngaert K, Edmundson GK, Stock RG, Stone NN, Yu Y, Zelefsky MJ. Intraoperative planning and evaluation of permanent prostate brachytherapy: Report of the American Brachytherapy Society. International Journal of Radiation Oncology Biology Physics. 2001; 51(5):1422–1430.
4. Narayanan S, Cho PS, Marks RJ. Fast cross-projection algorithm for reconstruction of seeds in prostate brachytherapy. Medical physics. 2002; 29(7):1572. [PubMed: 12148740]
5. Tutar IB, Managuli R, Shamdasani V, Cho PS, Pathak SD, Kim Y. Tomosynthesis-based localization of radioactive seeds in prostate brachytherapy. Medical physics. 2003; 30(12):3135. [PubMed: 14713080]
6. Kaplan ID, Meskell P, Oldenburg NE, Saltzman B, Kearney GP, Holupka EJ. Real-time computed tomography dosimetry during ultrasound-guided brachytherapy for prostate cancer. Brachytherapy. 2006; 5(3):147–151. [PubMed: 16864065]
7. Fuller DB, Jin H. Computed tomography-ultrasound fusion brachytherapy: Description and evolution of the technique. Brachytherapy. 2007; 6(4):272–279. [PubMed: 17964222]
8. Jain AK, Deguet A, Iordachita I, Chintalapani G, Blevins J, Le Y, Armour E, Burdette EC, Song D, Fichtinger G. Intra-operative 3D guidance in prostate brachytherapy using a non-isocentric C-arm. Lecture notes in computer science. 2007:4792–4799.
9. Jain AK, Mustafa T, Zhou Y, Burdette EC, Chirikjian GS, Fichtinger G. FTRAC—A robust fluoroscope tracking fiducial. Medical physics. 2005; 32(10):3185. [PubMed: 16279072]

NIH-PA Author Manuscript

NIH-PA Author Manuscript

NIH-PA Author Manuscript

10. Vikal S, Jain AK, Deguet A, Song D, Fichtinger G. TU-EE-A3-03: Automated Segmentation of Radiographic Fiducials for C-Arm Tracking. Medical physics. 2006; 33(6):2208.
11. Vikal S, Jain AK, Deguet A, Song D, Fichtinger G. WE-C-330A-03: Seed Segmentation in C-Arm Fluoroscopy for Brachytherapy Implant Reconstruction. Medical physics. 2006; 33(6):2229.
12. Tubic D, Zaccarin A, Pouliot J, Beaulieu L. Automated seed detection and three-dimensional reconstruction. I. Seed localization from fluoroscopic images or radiographs. Medical physics. 2001; 28(11):2265. [PubMed: 11764031]
13. Su Y, Davis BJ, Herman MG, Robb RA. Prostate brachytherapy seed localization by analysis of multiple projections: Identifying and addressing the seed overlap problem. Medical physics. 2004; 31(5):1277. [PubMed: 15191320]
14. Ji Q, Costa MS, Haralick RM, Shapiro LG. An Integrated Linear Technique for Pose Estimation from Different Geometric Features. International Journal of Pattern Recognition and Artificial Intelligence. 1999
15. Siddon RL, Barth NH. Stereotaxic localization of intracranial targets. International Journal of Radiation Oncology, Biology, Physics. 1987; 13(8):1241–1246.
16. Haralick RM, Sternberg SR, Zhuang X. Image Analysis Using Mathematical Morphology. IEEE Transactions on Pattern Analysis and Machine Intelligence. 1987; (4):532–550. PAMI-9. [PubMed: 21869411]
17. Otsu N. A threshold selection method from gray-scale histogram. IEEE transactions on systems, man and cybernetics. 1978; 8:62.
18. Haralick, RM.; Shapiro, LG. Reading, Mass. Addison-Wesley Pub. Co.; 1992. Computer and robot vision.
19. Ballard DH. Generalizing the Hough transform to detect arbitrary shapes. Pattern Recognition. 1981; 13(2):111.
20. Canny J. A Computational Approach to Edge Detection. IEEE Transactions on Pattern Analysis and Machine Intelligence. 1986; (6):679–698. PAMI-8. [PubMed: 21869365]
21. Fischler MA, Bolles RC. Random sample consensus: a paradigm for model fitting with applications to image analysis and automated cartography. Communications of the ACM. 1981; 24(6):381–395.
22. Halir R, Flusser J. Numerically Stable Direct Least Squares Fitting of Ellipses. Proc. Int. Conf. in Central Europe on Computer Graphics. 1998
23. Xie Y, Ohya J. Efficient detection of ellipses from an image by a guided modified RANSAC. Proceedings of SPIE. 2009
24. Seber, GAF. Multivariate observations. Hoboken, N.J.: Wiley-Interscience; 2004.
25. Lee J, Labat C, Jain AK, Song DY, Burdette EC, Fichtinger G, Prince JL. REDMAPS: Reduced-dimensionality matching for prostate brachytherapy seed reconstruction. IEEE Transactions on Medical Imaging. 2011; 30(1):38–51. [PubMed: 20643600]
26. Kon RC, Kumar Jain A, Fichtinger G. Hidden seed reconstruction from C-arm images in brachytherapy. 3rd IEEE International Symposium on Biomedical Imaging: Nano to Macro. 2006
27. Lee J, Liu X, Jain AK, Song DY, Burdette EC, Prince JL, Fichtinger G. Prostate Brachytherapy Seed Reconstruction With Gaussian Blurring and Optimal Coverage Cost. IEEE Transactions on Medical Imaging. 2009; 28(12):1955–1968. [PubMed: 19605321]

NIH-PA Author Manuscript
NIH-PA Author Manuscript
NIH-PA Author Manuscript

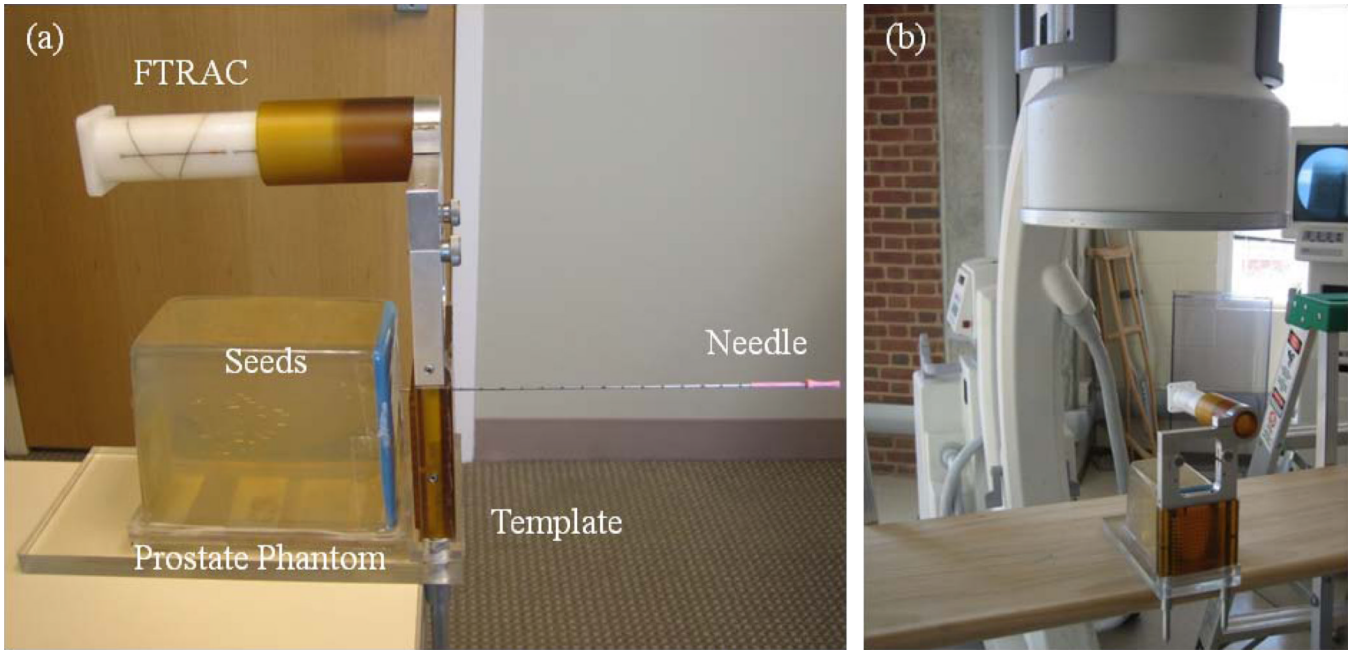

Fig. 1.
Phantom setup of the FTRAC. (a) Lateral view of the FTRAC setup. (b) Setup with non-isocentric mobile C-arm.

NIH-PA Author Manuscript

NIH-PA Author Manuscript

NIH-PA Author Manuscript

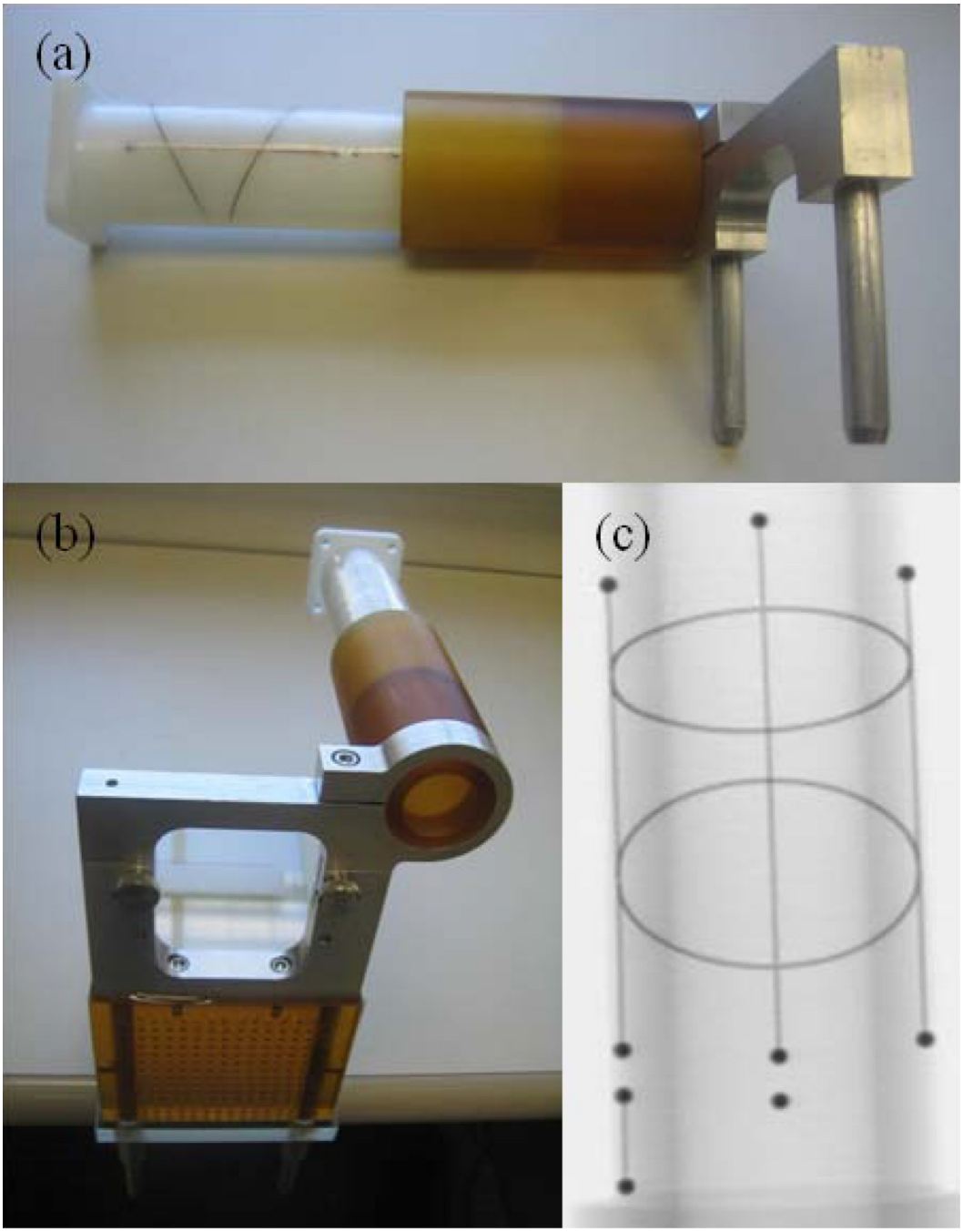

Fig. 2.
(a) FTRAC attached to the mounting bridge. (b) FTRAC mounted on needle template. (c) X-ray image of the FTRAC.

NIH-PA Author Manuscript
NIH-PA Author Manuscript
NIH-PA Author Manuscript

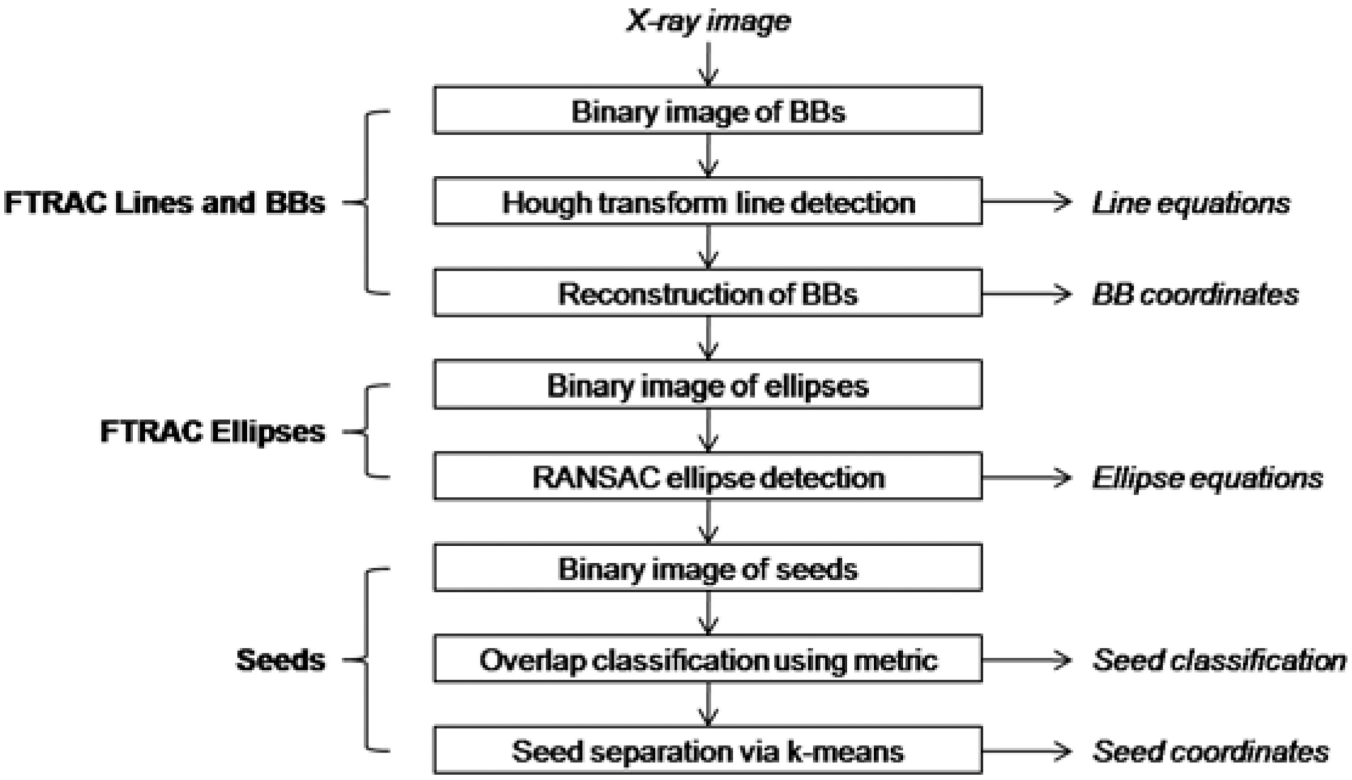

Fig. 3.
Flowchart of segmentation algorithm.

NIH-PA Author Manuscript
NIH-PA Author Manuscript
NIH-PA Author Manuscript

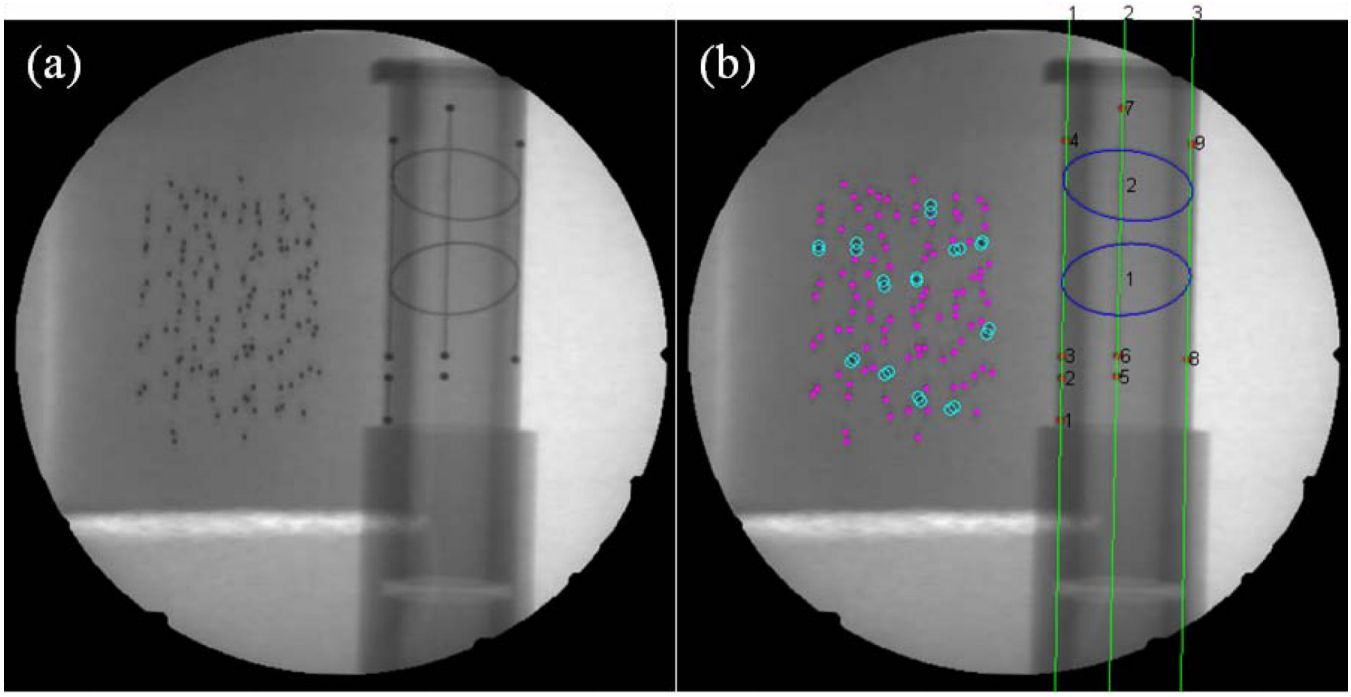

Fig. 4.
Sample phantom experiment segmentation. (a) Inputted original X-ray image. (b) Outputted segmentation of FTRAC lines (green), BBs (red dots), and ellipses (blue) as well as single (magenta dots) and overlapping (cyan circles) seeds overlaid on X-ray image.

NIH-PA Author Manuscript
NIH-PA Author Manuscript
NIH-PA Author Manuscript

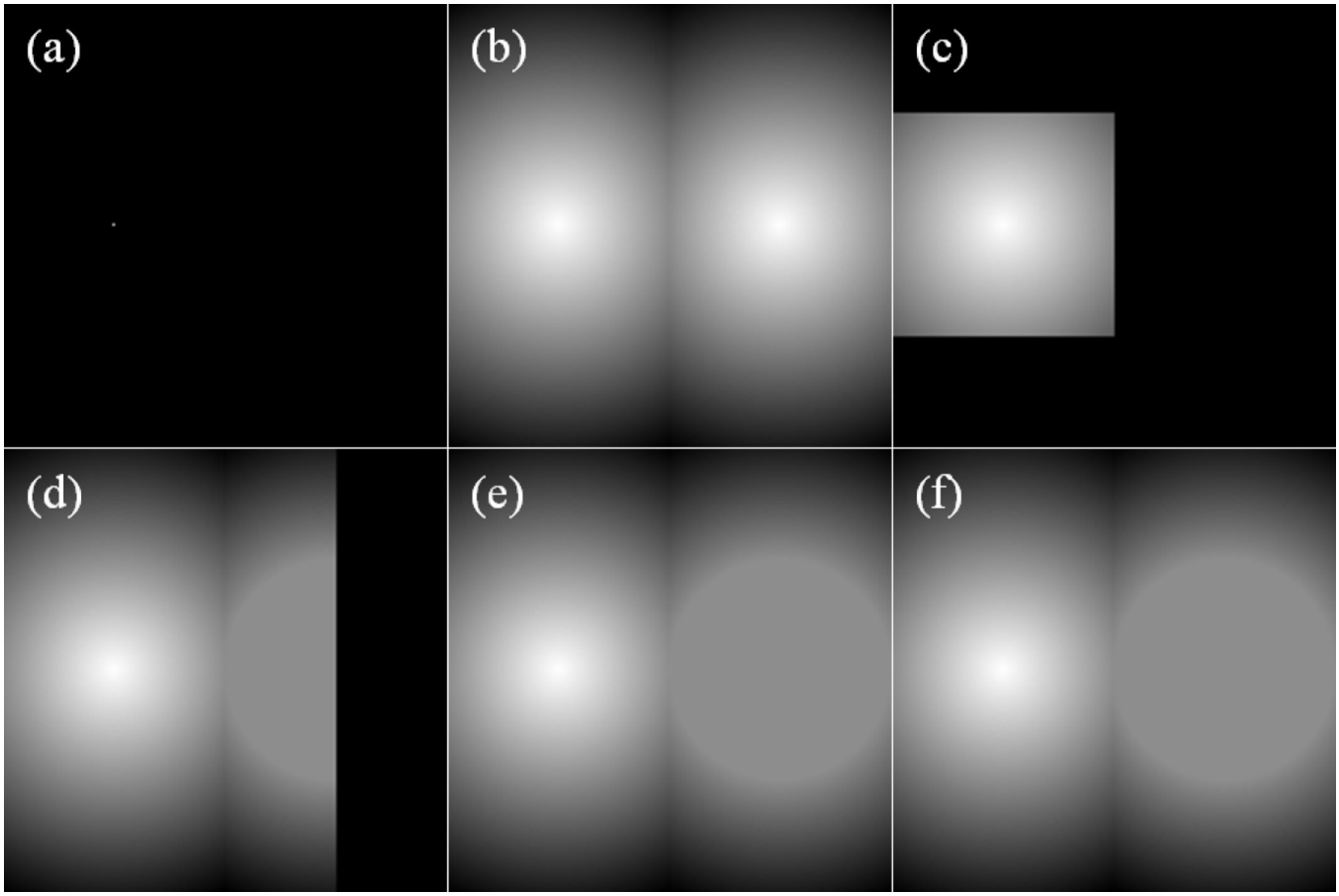

Fig. 5.

Grayscale examples of conditional dilation (using a 3×3 square structuring element) and reconstruction. (a) marker image, f^m. (b) mask image, f. (c) image after 50 conditional dilations, $\delta_B^{50}(f^m|f)$. (d) image after 100 conditional dilations, $\delta_B^{100}(f^m|f)$. (e) image after 150 conditional dilations, $\delta_B^{150}(f^m|f)$. (f) reconstructed image, $r_B(f^m|f)$.

NIH-PA Author Manuscript

NIH-PA Author Manuscript

NIH-PA Author Manuscript

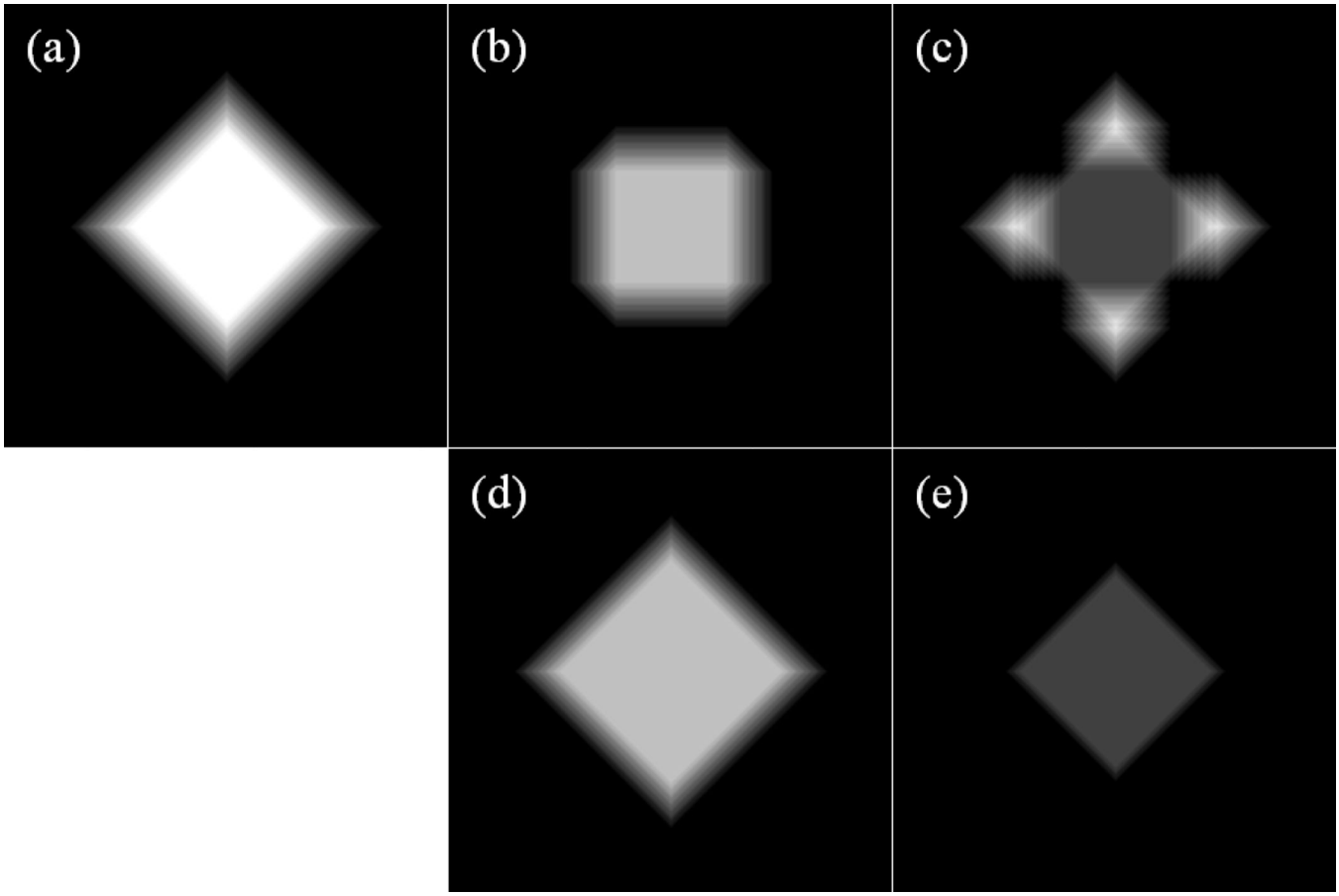

Fig. 6.

Grayscale examples of top-hat and top-hat by reconstruction (using a 50×50 square structuring element). (a) original image, f. (b) image after opening, $\psi_\delta(\psi_\varepsilon(f))$. (c) image after top-hat, $f - \psi_\delta(\psi_\varepsilon(f))$. (d) reconstructed image of opening, $r_B(\psi_\delta(\psi_\varepsilon(f))|f)$ (e) image after top-hat by reconstruction, $f - r_B(\psi_\delta(\psi_\varepsilon(f))|f)$.

NIH-PA Author Manuscript
NIH-PA Author Manuscript
NIH-PA Author Manuscript

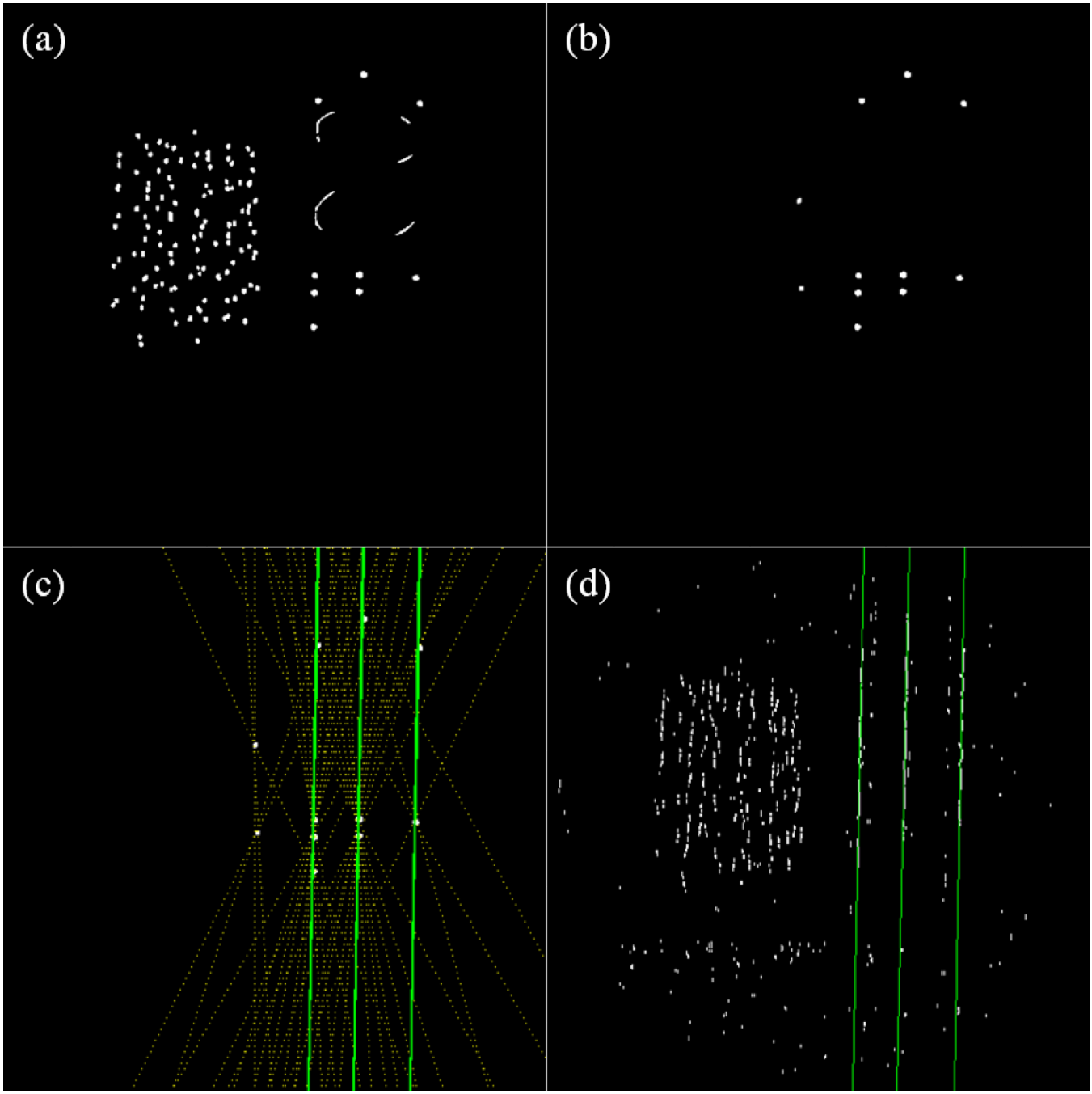

Fig. 7.
Sample phantom experiment FTRAC lines and BBs segmentation. (a) Binary BB image after applying Otsu's threshold. (b) Binary BB image after binary image processing. (c) FTRAC lines (green) selected from among roughly vertical Hough transform lines (yellow). (d) FTRAC lines better resolved by least squares fitting of detected vertical line edges.

NIH-PA Author Manuscript
NIH-PA Author Manuscript
NIH-PA Author Manuscript

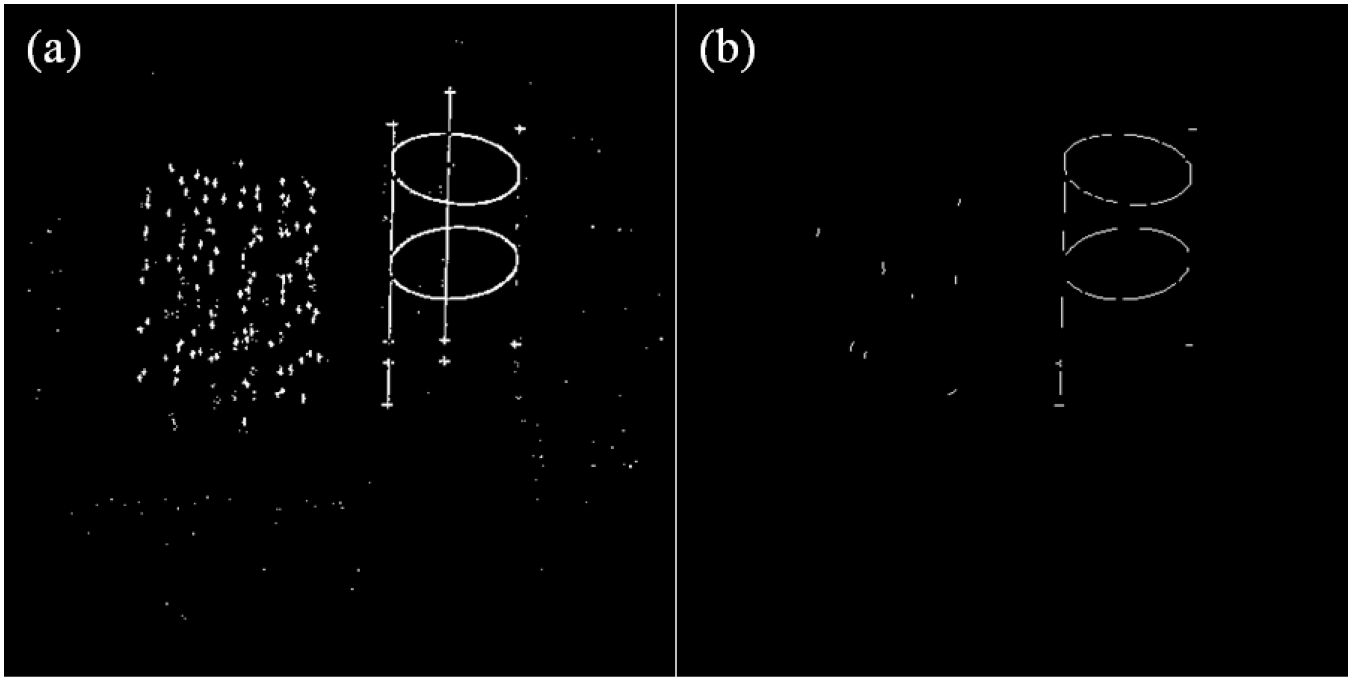

Fig. 8.
Sample phantom experiment FTRAC ellipses segmentation. (a) Binary ellipse edges image after applying Otsu's threshold. (b) Binary ellipse edges image after binary image processing.

NIH-PA Author Manuscript

NIH-PA Author Manuscript

NIH-PA Author Manuscript

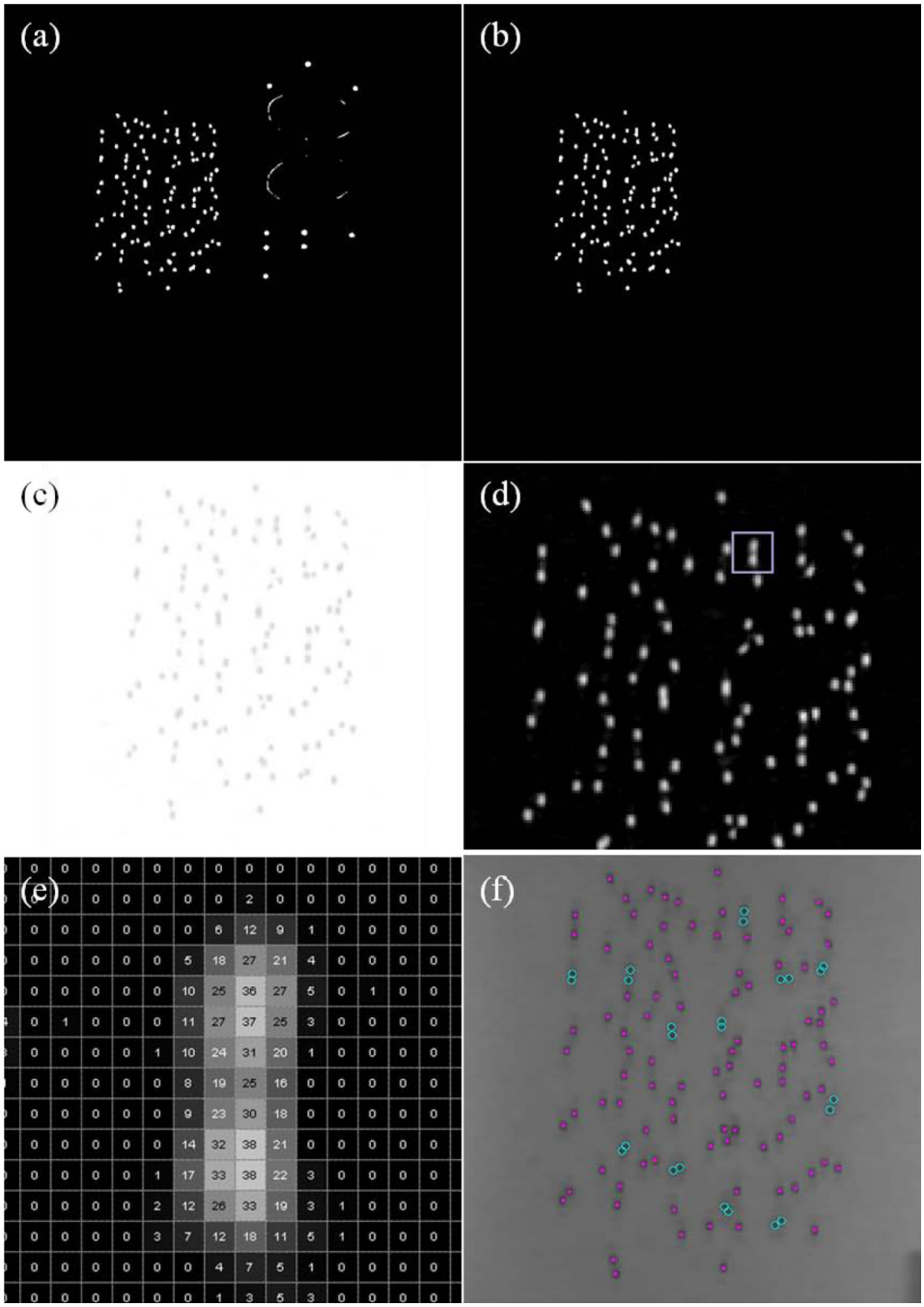

Fig. 9.

Sample phantom experiment seeds segmentation. (a) Binary seeds image after applying Otsu's threshold. (b) Binary seeds image after removing FTRAC. (c) Magnified complemented top-hat by reconstruction used to calculate metric for seed classification. (d) Magnified image of seeds with an example of overlapping seeds in rectangle. (e) Gaussian-like intensity distribution of overlapped seeds in rectangle of (d). (f) Magnified image of final seed segmentation.

NIH-PA Author Manuscript
NIH-PA Author Manuscript
NIH-PA Author Manuscript

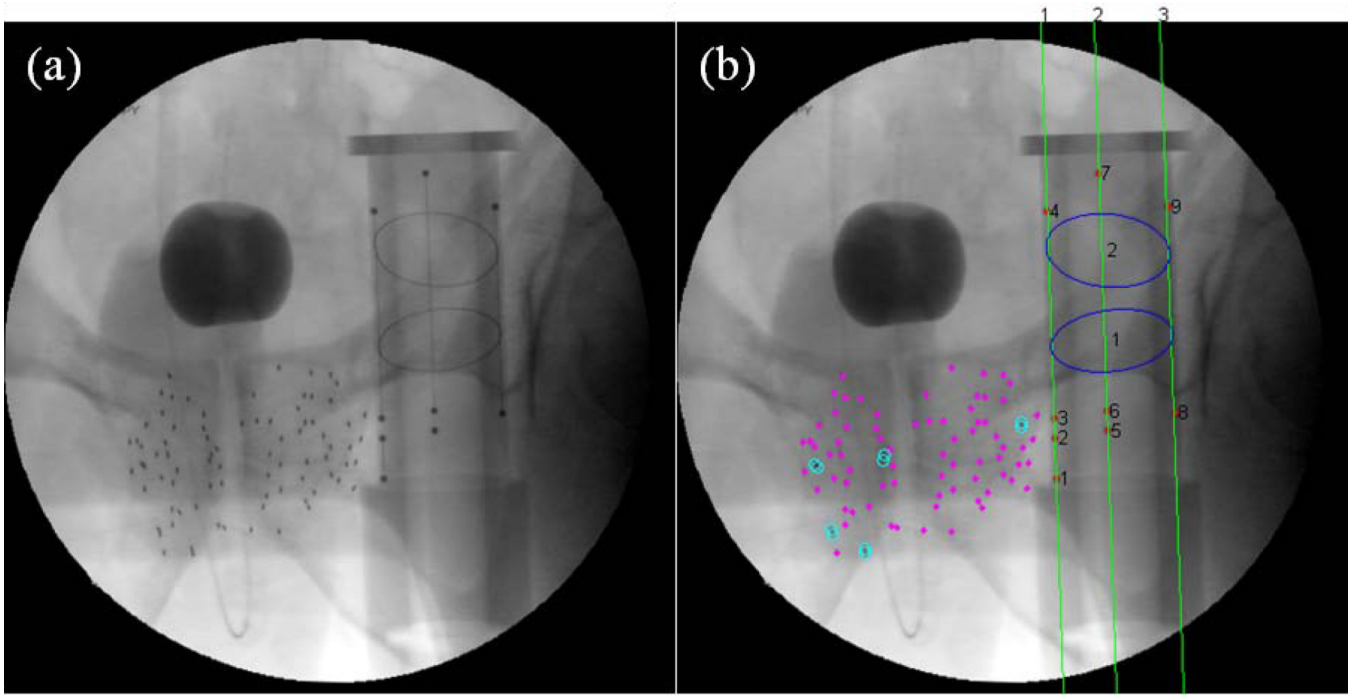

Fig. 10.
Sample clinical study segmentation. (a) Inputted original X-ray image. (b) Outputted segmentation of FTRAC lines (green), BBs (red dots), and ellipses (blue) as well as single (magenta dots) and overlapping (cyan circles) seeds overlaid on X-ray image.

NIH-PA Author Manuscript
NIH-PA Author Manuscript
NIH-PA Author Manuscript

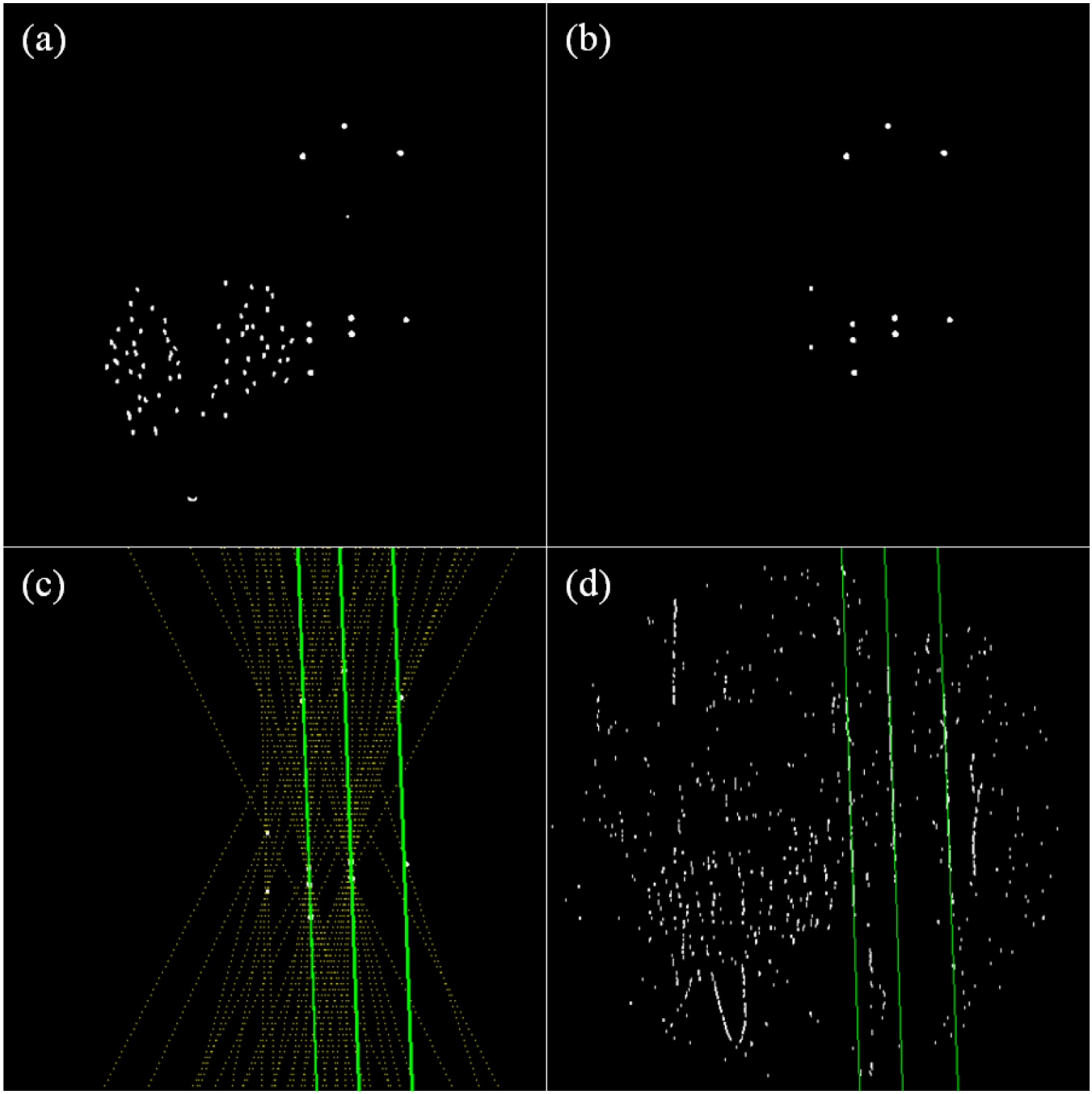

Fig. 11.
Sample clinical study FTRAC lines and BBs segmentation. (a) Binary BB image after applying Otsu's threshold. (b) Binary BB image after binary image processing. (c) FTRAC lines (green) selected from among roughly vertical Hough transform lines (yellow). (d) FTRAC lines better resolved by least squares fitting of detected vertical line edges.

NIH-PA Author Manuscript

NIH-PA Author Manuscript

NIH-PA Author Manuscript

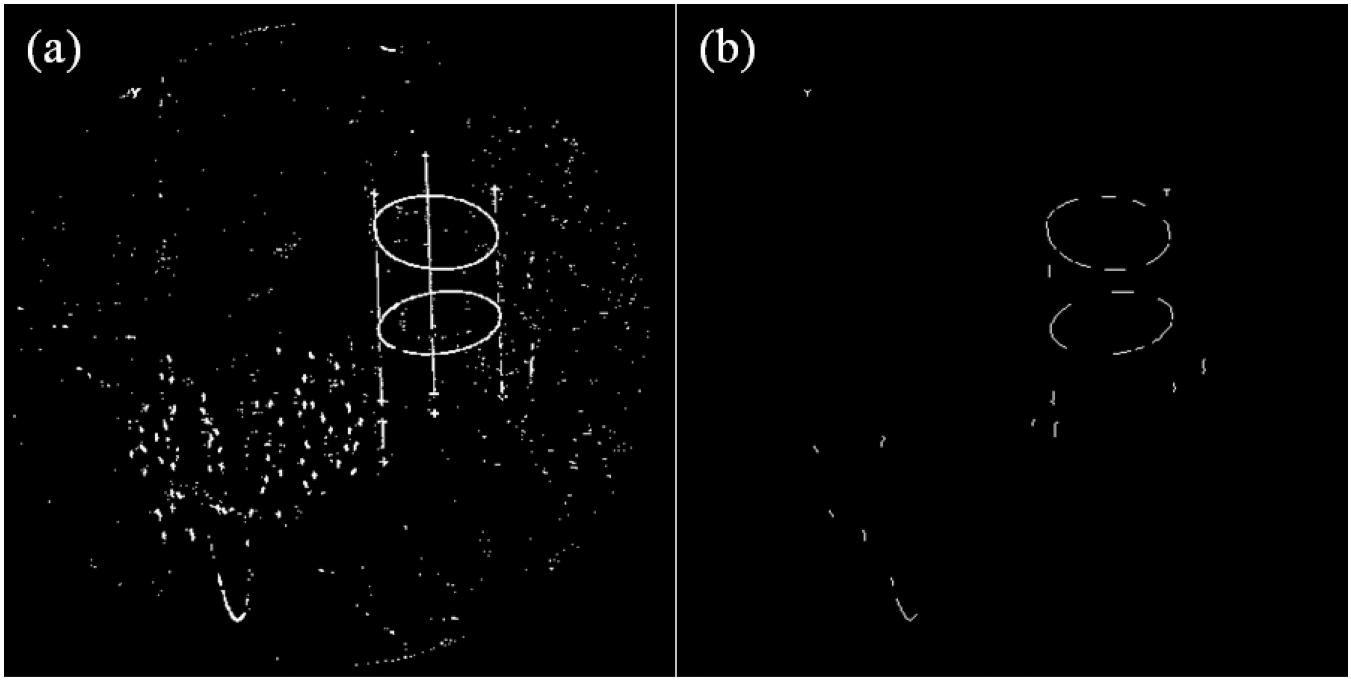

Fig. 12.
Sample clinical study FTRAC ellipses segmentation. (a) Binary ellipse edges image after applying Otsu's threshold. (b) Binary ellipse edges image after binary image processing.

NIH-PA Author Manuscript

NIH-PA Author Manuscript

NIH-PA Author Manuscript

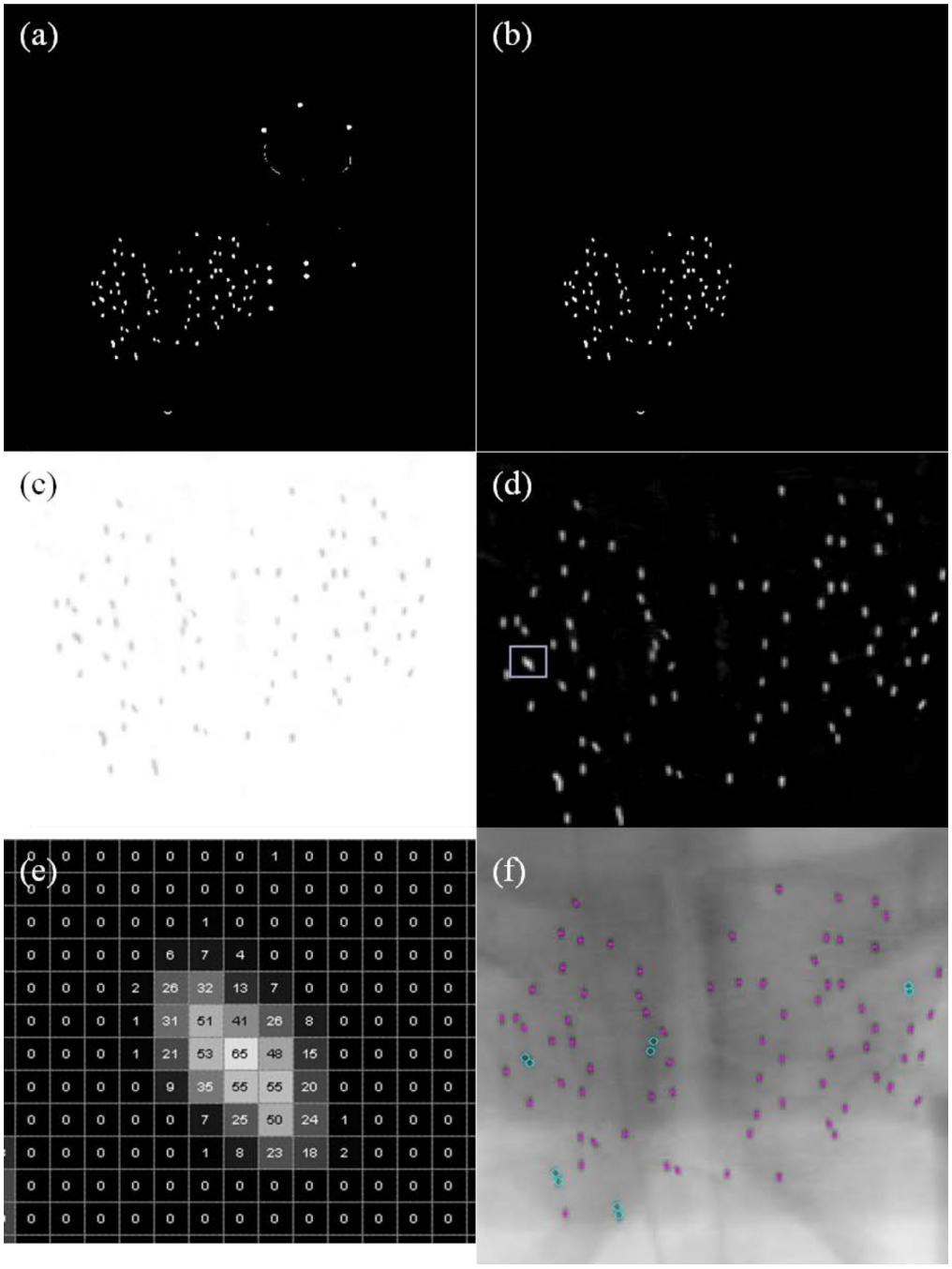

Fig. 13.

Sample clinical study seeds segmentation. (a) Binary seeds image after applying Otsu's threshold. (b) Binary seeds image after removing FTRAC. (c) Magnified complemented top-hat by reconstruction used to calculate metric for seed classification. (d) Magnified image of seeds with an example of overlapping seeds in rectangle. (e) Gaussian-like intensity distribution of overlapped seeds in rectangle of (d). (f) Magnified image of final seed segmentation.

NIH-PA Author Manuscript

NIH-PA Author Manuscript

NIH-PA Author Manuscript

Table 1

BB segmentation differences [root mean square (mm)].

BB #	Phantom	Clinical
1	0.2699	0.2431
2	0.3000	0.2464
3	0.2658	0.2405
4	0.2650	0.2635
5	0.2356	0.2332
6	0.2496	0.2616
7	0.1965	0.2759
8	0.1905	0.3038
9	0.1625	0.2481

NIH-PA Author Manuscript

NIH-PA Author Manuscript

NIH-PA Author Manuscript

Table 2

Line segmentation differences (mean ± std).

Data	Line #	Distance (mm)	Angle (degrees)
Phantom	**1**	0.3252 ± 0.2194	0.1314 ± 0.1114
	2	0.4521 ± 0.5130	0.2464 ± 0.2431
	3	0.6321 ± 0.4625	0.2304 ± 0.2077
Clinical	**1**	0.4260 ± 0.3798	0.2436 ± 0.2002
	2	0.4037 ± 0.3428	0.2566 ± 0.1928
	3	0.5269 ± 0.4018	0.2916 ± 0.2221

NIH-PA Author Manuscript
NIH-PA Author Manuscript
NIH-PA Author Manuscript

Table 3

Ellipse segmentation differences (mean ± std).

Data	Ellipse #	Center (mm)	Major axis (mm)	Minor axis (mm)	Orientation (degrees)
Phantom	**1**	0.2181 ± 0.0911	0.0970 ± 0.0773	0.0825 ± 0.0583	0.7119 ± 0.6463
	2	0.4136 ± 0.3598	0.4059 ± 0.5602	0.0919 ± 0.0819	0.5068 ± 0.6510
Clinical	**1**	0.2325 ± 0.1531	0.1952 ± 0.2821	0.1165 ± 0.1554	0.5861 ± 0.5163
	2	0.3462 ± 0.7220	0.2961 ± 0.7829	0.1558 ± 0.2112	0.8534 ± 1.0834

NIH-PA Author Manuscript

NIH-PA Author Manuscript

NIH-PA Author Manuscript

Table 4

Pose estimation differences (mean ± std).

Data	Rotation angle (degrees)	x (mm)	y (mm)	z (mm)
Phantom	0.3362 ± 0.2277	0.0698 ± 0.0481	0.0623 ± 0.0551	1.6546 ± 0.9500
Clinical	0.3965 ± 0.3228	0.0904 ± 0.0674	0.0925 ± 0.1316	2.1118 ± 2.7820

NIH-PA Author Manuscript

NIH-PA Author Manuscript

NIH-PA Author Manuscript

Table 5

Seed segmentation results.

Data	Patient	Number of Seeds	Detection Rate	False Positive Rate
Phantom	**Phantom**	20	98.1%	0.6%
		40	97.8%	0.3%
		60	97.3%	0.2%
		80	95.5%	0.0%
		100	94.9%	0.0%
		120	95.4%	0.3%
	Phantom Overall	-	95.9%	0.2%
Clinical	**1**	22	95.4%	3.7%
		44	99.3%	2.3%
		65	98.6%	2.7%
		66	98.9%	2.0%
	2	39	99.4%	2.0%
		82	98.9%	3.0%
		84	97.6%	2.9%
	3	33	99.6%	5.0%
		67	98.8%	3.0%
		70	99.0%	4.7%
	4	35	99.2%	4.1%
		68	99.7%	3.3%
		77	98.7%	1.6%
	5	24	100.0%	0.8%
		48	98.3%	1.7%
		53	99.0%	1.3%
	6	33	98.5%	0.8%
		61	99.8%	0.7%
		66	99.1%	0.9%
	7	81	99.5%	3.6%
	Clinical Overall	-	98.9%	2.6%